

Double K -shell ionization in the electron capture decay of ^{55}Fe

J. L. Campbell, J. A. Maxwell, and W. J. Teesdale

Guelph-Waterloo Centre for Graduate Work in Physics, University of Guelph, Guelph, Ontario, Canada N1G 2W1

(Received 28 September 1990)

The probability per K capture for double K -shell ionization in the electron capture decay of ^{55}Fe was obtained by fitting a model spectrum to the x-ray spectrum recorded to very high statistics in a high-resolution Si(Li) detector. The result, $P_{KK} = (1.3 \pm 0.2) \times 10^{-4}$, confirms the trend wherein experimental data decrease smoothly with Z , and are intermediate between the theoretical predictions of Intemann and of Suzuki and Law. Corrections to some recently published P_{KK} values reconcile them with this trend.

I. INTRODUCTION

When an atomic nucleus undergoes radioactive decay by K electron capture, there is a small probability that, as a result of the sudden change in nuclear charge, the second K electron will be ejected from the atom or excited to a higher atomic level. This process of double K vacancy creation has a very small probability ($P_{KK} = 10^{-4} - 10^{-5}$) but has attracted considerable interest. This is because of its very great sensitivity to correlation effects between the two bound K electrons in the initial state of the atom.

The calculation of P_{KK} is based upon the so-called sudden approximation and involves the calculation of the wave-function overlap between an initial K state having two bound K electrons and a final state with 2 K vacancies in the daughter atom together with an ejected continuum electron. For obvious reasons, the double-ionization process is often referred to as the "shakeoff". Double vacancies can also be created by the shakeup of a K electron to an unoccupied bound state, but the various theoretical treatments detailed below suggest that this is a negligible contributor to the overall probability of double-vacancy creation. In the shake-off process all the other electrons are regarded as frozen, but the more sophisticated theories take account of their effect, via shielding, upon the wave functions of the participating K electrons. The nuclear matrix elements cancel in the ratio of double to single K vacancy creation, reducing the calculation of P_{KK} to essentially the overlap integral calculation referred to above.

Two distinct trains of theoretical development are identifiable, each taking a particular approach to the treatment of the interaction between the initial K electrons and recent proponents of these two trains have joined forces in an attempt to integrate the two approaches.¹ Some 32 measurements on nuclides ranging from ^{37}Ar to ^{207}Bi have been reported,^{2,3} and it is clear that measurements based upon high-resolution x-ray spectrometers such as curved crystal spectrometers and Ge or Si detectors provide significantly lower P_{KK} values

than older low-resolution measurements. Presumably, the high-resolution results are less affected by radioactive contaminants. The tabulation of Isozumi,² restricted to high-resolution data, is therefore very useful.

Recent experiments^{4,5} on the atoms $Z = 25$ and 30 result in an interesting anomaly. These measurements, which employ two semiconductor x-ray detectors to seek coincidences between K x-ray pairs, provide P_{KK} values that are significantly larger than the predictions of the most sophisticated versions of the two theoretical approaches. In contrast, another Si(Li) detector result,⁶ this one for $Z = 26$ and based upon the single x-ray spectrum, gives a ratio that lies between the two predictions. This outcome is similar to the results of most other high-resolution measurements. Because of this discrepancy for a group of atoms of very similar atomic number, we have performed a new measurement for $Z = 26$, applying more sophisticated techniques for fitting x-ray spectra than have hitherto been used in this field.

II. THEORETICAL CALCULATIONS

The first calculation of P_{KK} was the pioneering work⁷ of Primakoff and Porter (PP) who calculated the wave-function overlap integral with nonrelativistic hydrogenic wave functions. Two simple factors were incorporated in the initial-state wave function to describe the effect of the mutual Coulomb interaction between the K electrons upon both the spatial correlation and the electrostatic shielding of the nuclear Coulomb force. The effective-charge parameters γ_1 and γ_2 in these factors were chosen to reproduce the Hylleras variational wave function for a two-electron atom.

The second train of development was initiated by Intemann and Pollock⁸ shortly after Pengra and Crasemann⁹ expressed concern about the possible inadequacies of the variational wave function. In this approach the initial-state electron-electron interaction is regarded instead as a perturbation of the nuclear Coulomb interaction, and the initial state is determined by perturbation theory, the K -shell correlation being described in

terms of the Coulomb propagator function. No free parameters are required to be assigned values in this method. Intemann and Pollock concluded that the differences between the variational wave-function method and their own Coulomb propagator method in describing the correlation effects were much less important than the nonrelativistic approximation made in both methods. Using a semirelativistic Hamiltonian, Intemann^{10,11} found that the inclusion of relativity decreased P_{KK} by a factor of 2.

The PP train of development continued with the work of Mukoyama *et al.*,¹² using fully relativistic hydrogenic wave functions. Initial-state correlation was accounted for by replacing Z in the hydrogenic wave functions by Z (effective) = $Z - \sigma$, where σ is a screening constant obtained from published self-consistent-field calculations. This work also demonstrated that the inclusion of relativistic effects results in a strong reduction in P_{KK} , but, again, the sensitivity to phenomenological parameters (screening constants) detracts from the value of the approach. For example, in the case of ⁵⁵Fe a relativistic hydrogenic calculation¹³ that omits correlation entirely generates a P_{KK} value that is six times larger than the Mukoyama *et al.* values. With the correlation effects of this magnitude, the ambiguity of the parameter-based methods used in the PP train of development confers a serious drawback on it.

For this reason, Suzuki and Law³ turned in the next development of the PP theme to a full many-body treatment based on a Dirac-Fock-Slater self-consistent-field (SCF) potential. These authors argued that, in view of the sixfold reduction of P_{KK} arising from the initial-state correlation, attention should also be paid to the hitherto neglected final-state correlation. Both correlations were described through the solution of the approximate SCF potential. The initial state was the conventional solution of the SCF equations. The final continuum state was determined numerically as the scattering state defined by the SCF potential for the daughter atom with 2 K vacancies. This final-state treatment was found to increase P_{KK} over the value otherwise calculated.

The theoretical situation may be summarized by examining the predictions for ⁵⁵Fe given in Table I. We restrict ourselves to relativistic calculations. Complete neglect of correlation effects (Ref. 13) gives $P_{KK} = 4.8 \times 10^{-6}$. The two alternative means of including initial-state correlations (Refs. 12 and 11) are in fair agreement, with a P_{KK} value reduced about fivefold. The addition of the final-state correlation by Suzuki and Law

(SL) has an opposite, but smaller, effect, restoring P_{KK} to about half the noncorrelated value. This cancellation of opposing large effects demonstrates that P_{KK} is very sensitive indeed to any residual correlation effects not catered for in the SL treatment.

Finally, the two trains of development have been merged by Intemann, Law, and Suzuki in a new relativistic approach¹ where the two initial K electrons are taken to experience the nuclear Coulomb potential, their own mutual interaction, and an effective central potential due to all other electrons, derived self-consistently. The two-electron wave function was obtained by a saddle-point variational method employing a Coulomb-constrained, correlation-split trial function based on hydrogenic forms. The final state is the same as in the SL treatment. The result of this method for ⁵⁵Fe is not very different from the propagator result of Intemann; given the inclusion of final-state correlations, this similarity suggests an even stronger reduction of P_{KK} due to this hybrid treatment of the initial-state correlation.

III. MEASUREMENTS

At first glance the requirement to detect and quantify a very weak x-ray satellite (intensity $\sim 10^{-4}$) in the presence of the diagram line (intensity = 1) at a nearby energy suggests the use of a high-resolution, and hence wavelength-dispersive, x-ray spectrometer. The concomitant low detection efficiency of such a device would then necessitate an inconveniently intense radioactive source. Instead, recent measurements have all employed semiconductor x-ray spectrometers, which are energy dispersive and combine modest resolution with high detection efficiency. This has allowed the use of weak radioactive sources which are not prone to self-absorption effects. However, it has not been considered feasible to observe the hypersatellite directly in Si(Li) or Ge detector spectra because of its proximity (see Fig. 1) to the high-energy side of the $K\beta_{13}$ line. Instead, two detectors have been operated in coincidence so that any K x-ray observed in the first detector "gates on" the second detector to look for a simultaneously emitted K x-ray. The peak-to-background problem is much ameliorated and the hypersatellite is visible when the observed coincidence spectrum in detector 2 is corrected by subtracting the simultaneously measured spectrum of random coincidences. Naturally the coincidence rate is low and the duration of the measurements has to be many weeks.

A main objective here is to check the coincidence re-

TABLE I. Values for P_{KK} for ⁵⁵Fe from relativistic calculations.

P_{KK}	Method	Reference
4.8×10^{-4}	Correlation effects neglected	13
0.881×10^{-4}	Initial state correlation by screening constant	12
1.13×10^{-4}	Coulomb propagator method	11
2.4×10^{-4}	SCF potential plus final-state correlation	3
0.904×10^{-4}	Correlation-split wave function	1

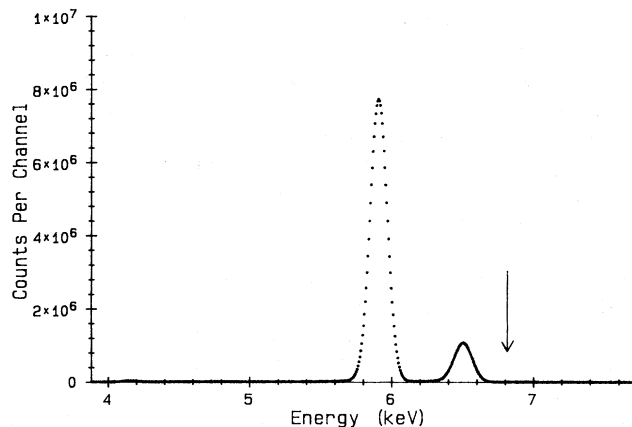


FIG. 1. Manganese K x-ray spectrum from ^{55}Fe decay recorded using a Si(Li) spectrometer. The position of the weak KK hypersatellite is indicated by the arrow.

sults for ^{54}Mn and ^{65}Zn , which are internally consistent but could conceivably share a common systematic error. We therefore did not emulate such measurements but, instead, measured the x-ray spectrum directly in a single Si(Li) detector; this approach was predicated on the view that, with sufficiently high-counting statistics and an accurately known resolution function, it should be possible to extract an acceptably accurate hypersatellite intensity by least-squares fitting the spectrum. This is precisely the approach we used to determine the intensity ($\sim 10^{-3}$) of the $K-L_1$ dipole-forbidden line in high- Z atoms using a GE detector.¹⁴ That line resides 500–800 eV lower than the $K\alpha_2$ peak and its extraction is made more difficult by low-energy tailing of the $K\alpha_2$ peak due to detector imperfections. The present problem concerns the high-energy side of the $K\beta_{13}$ line where, in a Si(Li) detector, no distortion due to imperfections is expected.

The source was a very thin layer of ^{55}Fe on a nickel backing having activity 4 mCi within a circular area of diameter 7.2 mm. From the manufacturer's estimate of specific activity at the time of manufacture, we estimate the equivalent iron thickness to be at most 3 mg/cm².

The detector was a specially selected "series E" detector, manufactured by Link Analytical. Its active area was limited to about 20 mm² by an internal tantalum collimator but, in order to blank off the periphery where the peak shape deteriorates, we added a 3-mm-diam external collimator. Scans of a pencil of monoenergetic iron $K\alpha_1$ x rays across a diameter had indicated that the low-energy tailing contribution to the line shape was minimum and uniform within the central area so defined. En route to the Si(Li) detector, the ^{55}Fe photons traversed 3.3 cm of air, a 0.0025-cm beryllium window and a nickel contact of thickness 14.5 nm. The electronic system comprised a Link 2040 Pulse Processor, a Nuclear Data 575 analog-to-digital converter (ADC), and a Nuclear Data 595 Digital Stabilizer. The processor is equipped with an efficient pileup rejection. The stabilizer

prevented degradation of the line shape due to small electronic drifts.

The hypersatellite intensity is very small, and so very high spectral intensity must be accumulated to render its statistical error tolerably low. This suggests the use of a high-counting rate. However, the experiment hinges on an accurate fitting of the region of the spectrum just to the right of the $K\beta$ x-ray peak, a region which is dominated by the Lorentzian "skirt" of that peak. An excessive counting rate causes tail pileup; i.e., some pulses are superposed upon the long-duration overshoot or undershoot from a preceding pulse, and this effect distorts the peak in a manner that mimics the Lorentzian skirt. Starting at 4000 s⁻¹, the counting rate was diminished and a corresponding diminution in the fraction of counts in the channel region 1300–1500 was noted. At rates below 1000 s⁻¹ there was no significant pileup augmentation of this portion of the spectrum. Two spectra for full fitting and analysis were then acquired at rates of 700 and 900 s⁻¹, each containing about 220×10^6 counts.

In order to determine the intrinsic line shape of the Si(Li) spectrometer, monoenergetic x-ray lines were provided by a curved crystal monochromator. We have described this procedure elsewhere¹⁵ for earlier detectors and, in this case, $K\alpha_1$ lines of titanium, chromium, iron, nickel, and copper were used to study the energy region of interest.

IV. LEAST-SQUARES ANALYSIS OF SPECTRA

A. Line-shape model

The analytic function used by us¹⁶ to describe the response of the present Si(Li) detector to a monoenergetic x-ray line in the energy region 3–20 keV is

$$F(i) = G(i) + D(i) + S(i) + S_T(i) + G_e(i), \quad (1)$$

where the components are Gaussian:

$$G(i) = H_G \exp \left[-\frac{(i - i_0)^2}{2\sigma^2} \right], \quad (2)$$

exponential:

$$D(i) = \frac{1}{2} H_D \exp \left[\frac{i - i_0}{\beta} \right] \operatorname{erfc} \left[\frac{i - i_0}{\sigma\sqrt{2}} + \frac{\sigma}{\beta\sqrt{2}} \right], \quad (3)$$

shelf:

$$S(i) = \frac{1}{2} H_S \operatorname{erfc} \left[\frac{i - i_0}{\sigma\sqrt{2}} \right], \quad (4)$$

truncated shelf:

$$S_T(i) = \frac{1}{2} H_{St} \left[\operatorname{erfc} \left[\frac{i - i_0}{\sigma\sqrt{2}} \right] - \operatorname{erfc} \left[\frac{i - i_T}{\sigma\sqrt{2}} \right] \right], \quad (5)$$

and escape peak:

$$G_e(i) = H_e \exp \left[-\frac{(i - i_e)^2}{2\sigma^2} \right]. \quad (6)$$

i represents the channel number, i_0 is the Gaussian cen-

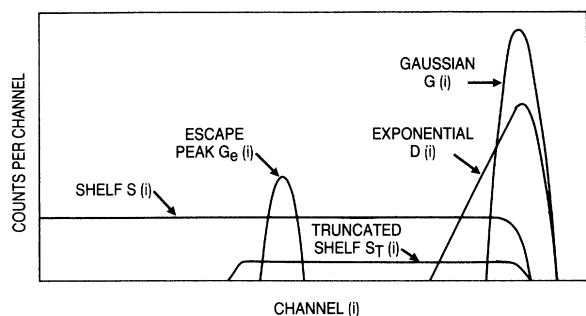


FIG. 2. Components of the line-shape function.

troid, i_e is the escape peak centroid, and i_T is the channel where the truncated shelf has fallen to half its height. The H parameters are the heights of the various components and β determines the slope of the exponential tail. The complementary error functions arise from the convolution of simple flat shelf and exponential terms with a unit-area Gaussian to remove nonphysical sharp edges. Figure 2 shows this function whose form is well justified by nonlinear least-squares fits to the measured monoenergetic lines; an example of such a fit is shown in Fig. 3, the reduced chi-squared per 10^6 counts in this case (iron) being 1.18.

As Fig. 3 makes clear, this representation suffices over a wide energy region. In the work described below, the

region of fit did not include the escape peaks of $K\alpha$ and $K\beta$, and so there was no need to distinguish between the two flat shelves. Accordingly, a single flat shelf $S(i)$ was employed in fitting ^{55}Fe data.

B. Fits of the ^{55}Fe spectrum

The dominant features of the spectrum, shown in Fig. 1, are the $K\alpha$ and $K\beta$ lines; although these are doublets, the doublet spacing is sufficiently small compared to the resolution [full width at half maximum (FWHM)] that each may be treated as a single line. The shape of each line is the convolution $F*L$ of the intrinsic Lorentzian line shape

$$L(i) = \frac{\Gamma/2\pi}{(i-i_0)^2 + (\Gamma/2)^2} \quad (7)$$

with the detector line shape $F(i)$. Because the intrinsic linewidth Γ is small compared to the FWHM, the convolution changes $F(i)$ negligibly in the main central region but imparts high- and low-energy tails. This results in a pronounced "skirt" to the right of the $K\beta$ line and also explains why the low-energy tails of the two lines are significantly more intense than the tails observed in the monoenergetic data.

Further complications arise due to the radiative Auger effect, a process where the K excitation energy is shared between an x-ray photon and a loosely bound orbital electron which is ejected from the atom. These x-ray events result in satellites just to the left of $K\alpha$ and $K\beta$. Theoret-

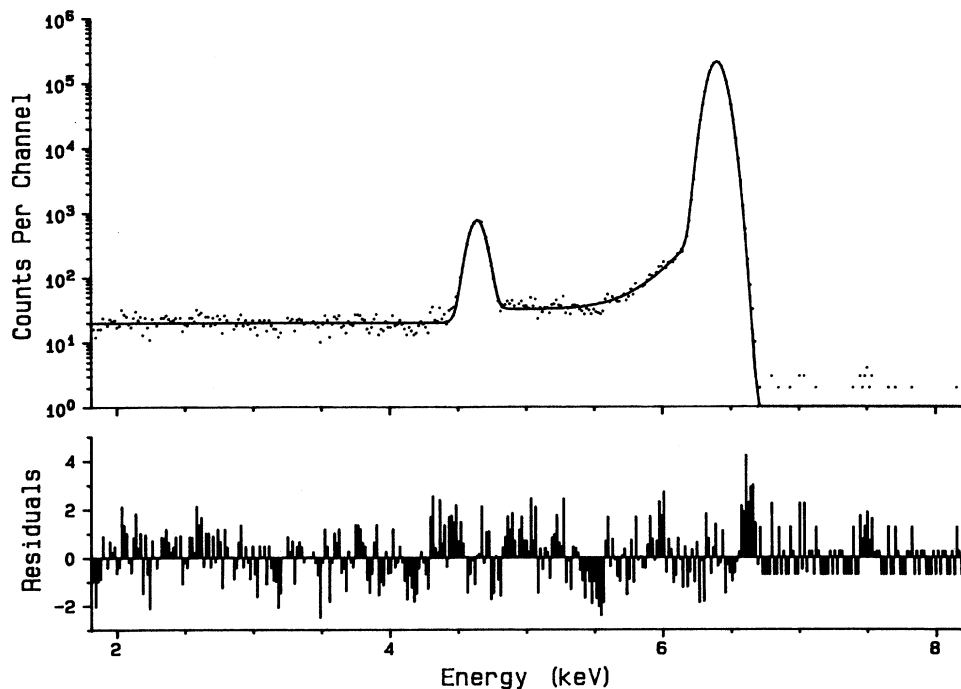


FIG. 3. Details of the fit to a monoenergetic x-ray line of energy 6.40 keV. The upper plot shows the data (dots) and the fit. The lower plot shows the residues in units of one standard deviation. The silicon escape peak is displaced 1.75 keV to the left of the main peak.

ical¹⁷ and measured¹⁸ satellite intensities are only in rough agreement, reflecting the low intensity ($\sim 0.5\%$ for $K\alpha$, 2.4% for $K\beta$) and the difficulty of discerning these even in wavelength-dispersive spectroscopy. Nevertheless, in the present work, where goodness of fit is crucial, these should be included in the model spectrum. This is done by placing additional (Gaussian) lines at energies of 5.80 and 6.40 keV. Admittedly, this is only an approximate representation since wavelength-dispersive spectroscopy shows the $K\beta$ satellite to be a broad distribution extending 250 eV to the left of its parent peak. However, it appears (see below) that the portion of the distribution not represented by the Gaussian can be satisfactorily absorbed by the tail component $D(i)$ if its parameters are permitted to vary.

The process of K electron shakeoff during K capture will give rise to very weak $K\alpha$ and $K\beta$ hypersatellite lines. It is only feasible to observe the $K\beta$ hypersatellite whose energy is calculated¹⁹ as 6.816 eV. There is also the possibility of L electron ionization during K capture; the resulting $K\beta$ satellite is at 6.56 keV.

The two principal features of the model spectrum are then the $K\alpha$ peak and its KLM satellite, and the $K\beta$ peak together with its KMM satellite and the KL peak arising from L shakeoff. These two groups are sufficiently separate in energy that, according to the monoenergetic x-ray fits, they will have distinct shelf and tail components, but there will be no significant variation within each group. Accordingly, the $K\alpha$ group was assigned one tail and one shelf, and the $K\beta$ group a different tail and shelf; six variable parameters are thus introduced. Within the $K\beta$ group, the only peak height varied was that of the $K\beta_{13}$ line; the KMM satellite intensity was held at 2% of that of $K\beta_{13}$ following empirical variation to find the best fit and the KL satellite was fixed at 0.25% of $K\beta_{13}$ in accord with the experimental results of Li-Scholz *et al.*²⁰ Turning to the $K\alpha$ group, it was found that the assignment of a separate KLM peak had no effect on the results and so that peak was dropped and the tail component $K(i)$ left to absorb it.

The feature that is the focus of interest is the KK hypersatellite, which is represented by a Gaussian of variable height. The remaining features obvious to visual inspection are K x-ray peaks of nickel and the $K\beta$ peak of iron. The nickel lines arise from the excitation of the detector contact; they are included in the model as a doublet of fixed-intensity ratio with the $K\alpha$ height as the sole variable. The iron $K\beta$ line, which presumably is due to self-excitation of source material and of iron impurity in the beryllium window, was represented by a single Gaussian; the corresponding iron $K\alpha$ line would not be statistically significant.

To the five peak heights and the six tailing parameters indicated, we add four further variables $a-d$ arising from the two calibration equations. The first reflects the linear relationship of the centroid channel to the x-ray energy and the second the dependence of the Gaussian width on the x-ray energy:

$$(i_0)_k = a + bE_k, \quad (8)$$

$$(\sigma^2)_k = c + dE_k. \quad (9)$$

These features are superposed on a background due to cosmic rays and environmental gamma radiation. On the basis of separate measurements, this is taken to be horizontal and its height is a variable of the fit.

We noted above that the $K\alpha$ and $K\beta$ lines are properly represented by the convolution of a Lorentzian distribution $L(i)$ by the quasi-Gaussian detector line shape $F(i)$. This convolution has always been neglected in Si(Li) spectroscopy, but, in the present case where the resolution is excellent and the statistics very high, this neglect would cause a poor fit in the crucial region of the spectrum containing the KK satellite. The convolution is accomplished numerically in each iteration of the fitting procedure. The approach that first comes to mind is to construct the initial Lorentzian distribution and then to redistribute the contents $L(i)$ of each channel by computing the function $F(i)$ having total intensity $L(i)$ counts. Since several parameters of $F(i)$, namely, σ , β , H_D , and H_S , are energy dependent, $F(i)$ has to be reevaluated at every channel, making the convolution computationally intensive. Therefore, the opposite, but entirely equivalent, approach is adopted whereby the distribution $F(i)$ is first constructed and then each channel is redistributed with the same $L(i)$ function.

Linewidths^{21,22} for the K x rays of transition metals have been measured via the FWHM of K lines observed in wavelength-dispersive spectroscopy and are much larger than values derived by taking the sum of theoretically calculated atomic level widths. This reflects that fact that there are a variety of sources of line broadening in addition to the natural width. It is important to note that the extreme outer regions of the Lorentzian (high-frequency components) are only governed by the natural width. The slight error incurred in the central region of the peak is inconsequential; in fact, half of the error incurred by neglect of the Lorentzian has been eliminated. The actual linewidth values used²¹ were $\Gamma(K\alpha) = 1.48$ eV and $\Gamma(K\beta) = 1.20$ eV. The other spectral features, i.e., the hypersatellite, the iron, and the nickel x rays, had very low statistics and so convolution was unnecessary in these cases.

The last feature to be noted is a dip in the spectrum at energies between 7.1 and 7.4 keV. We attribute this to manganese x-ray absorption within the iron source material. From the manufacturer's specifications, the iron thickness is certainly less than 3 mg/cm^2 . Absorption of x rays arising from a uniform distribution of ^{55}Fe atoms in an iron layer of defined thickness was therefore built into the peak model. The main effect of the layer is the critical absorption of x rays in the Lorentzian high-energy tail at energies just above the iron K edge (7.06 keV). This edge was smeared by an appropriate Gaussian to represent the effect of detector resolution. We performed fits using various fixed thickness values between 1.5 and 3 mg/cm^2 and concluded that excellent fits were afforded by a value $2.2 \pm 0.2 \text{ mg/cm}^2$. Fortunately, P_{KK} proved to be only very slightly dependent upon this attenuation correction.

Finally, we emphasize that, in the fitting procedure, the tail and shelf parameters for each of the $K\alpha$ and $K\beta$

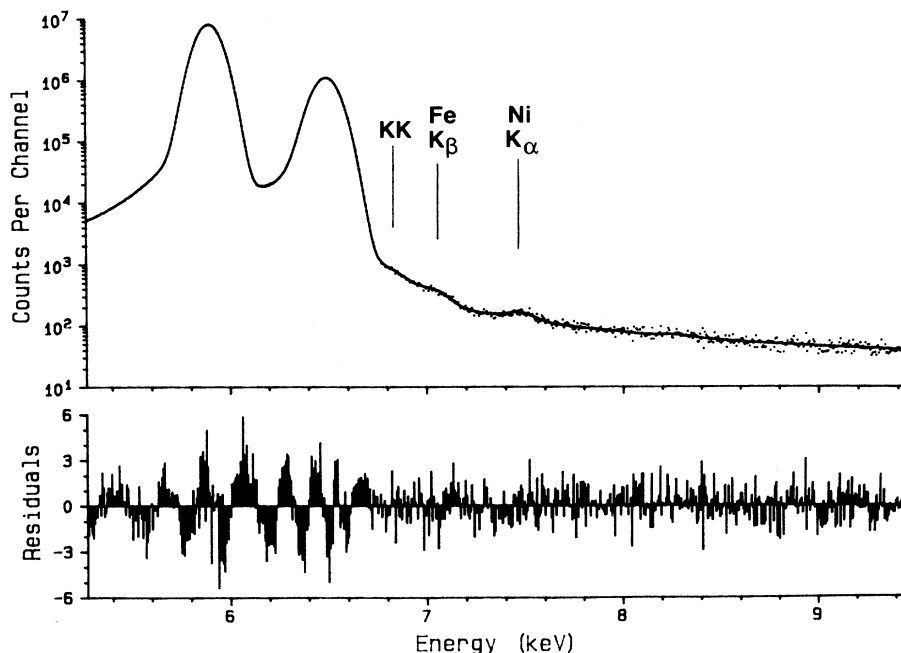


FIG. 4. Details of the fit to the ^{55}Fe spectrum. The upper plot shows the data (dots) and the fit. The lower plot shows the residues in units of one standard deviation. The iron $K\beta$ and nickel $K\alpha$ lines are visible to the right of the manganese $K\alpha$ and $K\beta$ lines; the Mn KK hypersatellite arising from double ionization is barely visible.

groups were variables. They were not fixed at the values given by fitting the monoenergetic calibration lines; these only served to justify the functional form. By permitting the parameters to vary, the long-term portions of the RA satellites, which are not explicitly catered to by Eqs. (2)–(6), can be absorbed into the tailing components. Slight enhancements of the ^{55}Fe tail intensities relative to monoenergetic peak values showed that this was happening.

Figure 4 displays the final fit to the spectrum recorded at 900 s^{-1} . This spectrum contains 220×10^6 counts and, since the reduced chi squared is a linearly increasing function of spectrum intensity, the value $\chi_r^2 = 2.1$ obtained represents an excellent fit.

V. DISCUSSION

Table II summarizes the measured ratio R of the $K\beta$ hypersatellite and diagram line intensities. This ratio is

given by

$$R = P_{KK} \frac{\omega_K^1 f_\beta^1}{\omega_K f_\beta} \quad (10)$$

in which ω_K is the conventional K -shell fluorescence yield and f_β the fractional intensity of the K_β line in the K x-ray series. The primed quantities are the analogues of these for the double-vacancy situation. All experiments to date in this field have been interpreted using the assumption that $\omega_K^1 = \omega_K$ and $f_\beta^1 = f_\beta$. We proceed on that basis for the moment, with the result that $P_{KK} = (1.3 \pm 0.2) \times 10^{-4}$. The immediate conclusion is that the previous result⁶ of $(1.2 \pm 0.4) \times 10^{-4}$ is verified, although the present result is perhaps to be preferred on the grounds of the sophistication of the spectrum analysis. Had the trend set by recent ^{54}Mn and ^{65}Zn results been followed, a ^{55}Fe result of 2.9×10^{-4} would have been expected. This appears to be precluded and, hence, some factor must be at work which causes the case

TABLE II. Experimental results.

Run no.	Peak intensities		
	$K\beta_{13}$	$KK (\pm 3\sigma)$	P_{KK}
1	2.757×10^7	3928 ($\pm 15\%$)	1.39×10^{-4}
2	2.663×10^7	3405 ($\pm 15\%$)	1.25×10^{-4}

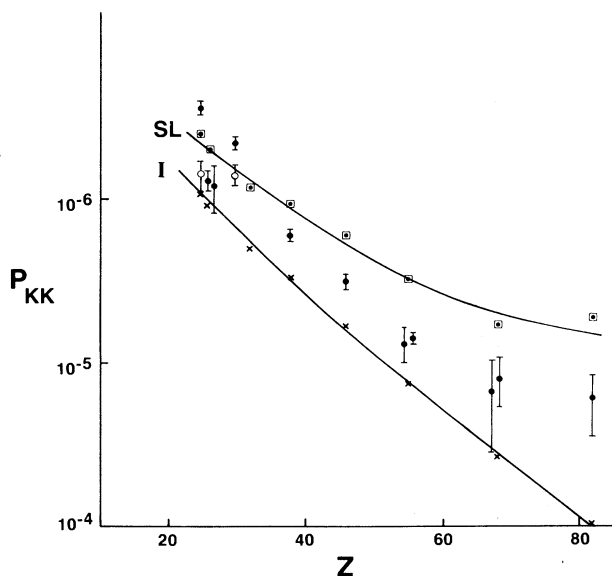


FIG. 5. Measured and calculated P_{KK} values. The open circles result from correcting published data for contributions from internal conversion.

of $Z = 26$ to differ from these nearby atoms at $Z = 25$ and 30.

We have drawn upon Isozumi's summary of high-resolution data to prepare Fig. 5, which compares these data with the predictions of the two culminating papers in the two lines of development; these are Intemann's Coulomb propagator approach¹¹ and the self-consistent-field treatment³ of Suzuki and Law. The upper curve is an approximate representation of the SL trend and the lower one of the Intemann trend; the factor of 2 difference at $Z = 25$ widens with increasing Z to a factor of 18 at $Z = 82$. We have omitted the two cases at $Z = 48$ and 74 for reasons that we develop later.

Eight of the experimental data points given by Isozumi fall between the two curves; our datum at $Z = 26$ agrees with the previous iron result but with its lower error strengthens the evidence for a smooth Z dependence of experimental results falling between the Intemann and SL treatments. The two experimental points^{4,5} that do not follow this trend are those for ^{54}Mn and ^{65}Zn . In the ^{54}Mn case, each electron capture (EC) event is followed within the coincidence resolving time by a nuclear electromagnetic transition of energy 835 keV. The authors of

Ref. 4 state that the internal conversion is a negligible source of K x rays but, using a K conversion coefficient value²³ of 2.2×10^{-4} , we calculate that 61% of observed KX - KX coincidences in this experiment are between the x rays from K capture and K conversion. The corrected P_{KK} value becomes $(1.4 \pm 0.3) \times 10^{-4}$, shown as an open circle in Fig. 5. There is a similar additional source of coincident K x rays in the decay of ^{65}Zn , although it is smaller here since only 50.6% of electron capture events have a coincident nuclear transition. The corrected P_{KK} value here is 1.37×10^{-4} , again shown as an open circle. It should be noted that in all other reported cases there are either no nuclear transitions or the coincident nuclear transition is an isomer so that x rays from its internal conversion do not occur within the coincidence resolving time.

Both of these corrected values follow the trend of all the other data points, so that a coherent picture emerges in which the Intemann treatment appears to generate overly low P_{KK} values and the SL treatment values that are too large. The effort¹ by these two groups of authors to pool their treatments is not successful, since the Intemann, Law, and Suzuki (ILS) predictions start out a little below the Intemann predictions at $Z = 25$ and fall below the Intemann curve with increasing Z .

The question of the equality of ω_K and ω_K^1 is currently being examined by Chen and Crasemann.²⁵ Their preliminary results suggest that ω_K^1 is some 6% larger than ω_K at $Z = 25$, and that the difference decreases with increasing Z . This effect is not large enough to change the above conclusions.

The two cases that were omitted from Fig. 5 are summarized in Table III. They are ^{109}Cd and ^{181}W , and they are characterized by very low values of electron capture decay energy (Q_{EC}) so that the decay energy is of the same order as the K -shell binding energy B_K . In these cases, both theoretical predictions fall far below the trend set by other nuclides; the experimental values do not fall between the predictions. There is a resemblance here to the analogous process of K -shell ionization in beta decay.² In that case, the shakeoff probability $P_K(\beta^-)$ falls off quite smoothly with increasing atomic number. But, in the few cases where the decay energy is not significantly greater than the K -shell binding energy, both predictions and experimental values fall well below the general trend. Nevertheless, there is good agreement between experiment and the predictions of the SCF theory of Law and Suzuki²⁴ whatever the ratio of decay energy to binding energy is.

TABLE III. P_{KK} data ($\times 10^{-5}$) for EC decays of very low decay energy.

	^{109}Cd	^{181}W
Q_{EC}/B_K	3.5	2.57
P_{KK} (Intemann)	0.34	0.022
P_{KK} (SL)	0.89	0.14
P_{KK} (experiment)	1.02 ± 0.36	0.24 ± 0.06

VI. CONCLUSIONS

The P_{KK} value of $(1.3 \pm 0.2) \times 10^{-4}$ measured here for the electron capture decay of ^{55}Fe agrees with the earlier measurement of $(1.2 \pm 0.4) \times 10^{-4}$. All but two measured values now fall on a smooth, decreasing trend with the atomic number intermediate between the predictions of the Intemann and SL theories. When corrections are made for K x rays contributed by the internal conversion process, the remaining two data points, previously anomalous, join this trend. The only exceptions are for two electron capture nuclides where the ratio Q_{EC}/B_K is only slightly larger than unity. New measurements for these two cases would be interesting. There is also a need for rigorous calculations of double-vacancy fluorescence yields in order to remove small errors incurred by the assumption of equal fluorescence yields for single and dou-

ble vacancies.

The composite ILS theory does not provide a satisfactory resolution of the situation, since its result resembles the Intemann values at low Z but fall rapidly below them as Z increases. It appears to overestimate the effects of the initial-state correlation, which conspires to decrease P_{KK} . Any new theoretical approach faces the challenge of fine tuning the large and opposing effects on P_{KK} stemming from initial- and final-state correlations.

ACKNOWLEDGMENTS

This work was supported by the Natural Sciences and Engineering Research Council of Canada. The issue of the double-vacancy fluorescence yield was brought to our attention by Professor Bernd Crasemann; we are in his debt for this advice and subsequent discussion.

-
- ¹R. L. Intemann, J. Law, and A. Suzuki, *J. Phys. Colloq.* **48**, C9-555 (1987).
²Y. Iozumi, *Nucl. Instrum. Methods* **A280**, 151 (1989).
³A. Suzuki and J. Law, *Phys. Rev. C* **25**, 2722 (1982).
⁴H. J. Nagy and G. Schupp, *Phys. Rev. C* **30**, 2031 (1984).
⁵H. J. Nagy and G. Schupp, *Phys. Rev. C* **27**, 2887 (1983).
⁶J. P. Briand, P. Chevalier, A. Johnson, J. P. Rozet, M. Tavemier, and A. Touati, *Phys. Lett.* **49A**, 51 (1974).
⁷H. Primakoff and F. T. Porter, *Phys. Rev.* **89**, 930 (1953).
⁸R. L. Intemann and F. Pollock, *Phys. Rev.* **157**, 41 (1967).
⁹J. G. Pengra and B. Crasemann, *Phys. Rev.* **131**, 2642 (1963).
¹⁰R. L. Intemann, *Phys. Rev.* **178**, 1543 (1969).
¹¹R. L. Intemann, *Phys. Rev. C* **3**, 1961 (1985).
¹²T. Mukoyama, Y. Iozumi, T. Kitahara, and S. Shimizu, *Phys. Rev. C* **8**, 1308 (1973).
¹³J. Law and J. L. Campbell, *Nucl. Phys.* **A199**, 481 (1973).
¹⁴J. L. Campbell, P. L. McGhee, J. A. Maxwell, R. W. Ollerhead, and B. Whittaker, *Phys. Rev. A* **33**, 986 (1986).
¹⁵J. L. Campbell, A. Perujo, and B. Millman, *X-ray Spectrom.* **16**, 195 (1987).
¹⁶J. L. Campbell and J. X. Wang, *X-Ray Spectrom.* (in press).
¹⁷H. Scofield, *Phys. Rev. A* **9**, 1041 (1974).
¹⁸E. Marageter, W. Wegscheider, and K. Müller, *X-Ray Spectrom.* **13**, 78 (1984).
¹⁹M. H. Chen, B. Crasemann, and H. Mark, *Phys. Rev. A* **25**, 391 (1982).
²⁰A. Li-Scholz, A. Leiberich, and W. Scholz, *Phys. Rev. A* **26**, 3232 (1982).
²¹M. O. Krause and J. H. Oliver, *J. Phys. Chem. Ref. Data* **8**, 329 (1979).
²²B. Ekstig, E. Källne, E. Noreland, and R. Manne, *Phys. Scr.* **2**, 38 (1970).
²³*Table of Isotopes*, 7th ed., edited by C. M. Lederer and V. S. Shirley (Wiley, New York, 1978).
²⁴J. Law and A. Suzuki, *Phys. Rev. C* **25**, 514 (1982).
²⁵B. Crasemann and M. H. Chen, private communication.